Near-field dynamics at a metallic transmission grating with femtosecond illumination: A theoretical study

Roland Müller and Jens Bethge[*]
Max Born Institute, Max-Born-Straße 2a, D-12489 Berlin

(Received 19 January 2018; published 22 August 2018)

This paper reports on the temporal and spectral light field evolution for two different types of metallic gratings after illumination with a near-infrared TM-polarized femtosecond pulse: a freestanding grating in air and a grating on a dielectric substrate. The electromagnetic field components are calculated numerically at various transverse locations of the gratings by use of a finite-difference time-domain model. The spectral dynamics are explained by the dynamics of surface plasmon polaritons (SPPs). Fano-like profiles are observed close to an SPP resonance in the calculated spectral curves, indicating a connection between the Rayleigh anomaly and a nearby SPP resonance. For the freestanding grating, only a single Fano-like profile close to the air/metal SPP resonance and, with the dielectric support, two Fano-type profiles are observed, one in the proximity of the air/metal SPP resonance, the other in the proximity of the substrate/metal resonance. Investigating the changes in the spectra for an increasing distance to the grating, it is found that with increasing distance, the spectral curves related to different transverse locations coincide almost completely, providing evidence that the near-field contributions disappeared.

DOI: 10.1103/PhysRevB.98.085428

I. INTRODUCTION

Optical properties of metallic nanostructures have been intensively studied during the last four decades. One important finding is that the light/metal interaction can, in many cases, be explained with the presence of surface plasmon polaritons (SPPs) [1–4]. Novel optical effects have been discovered at the light-metal interaction on metallic films perforated by two-dimensional nanohole arrays [5–11] or on one-dimensional subwavelength slit apertures [12–18]. The work of Ebbesen *et al.* provides evidence for extraordinary optical transmission (EOT) through subwavelength hole arrays in opaque gold or silver thin films at particular wavelengths [5]. EOT refers to enhanced light transmission compared to the light transmission through hole arrays in a perfectly conducting thin-film. However, experimental and theoretical studies revealed that SPPs play an essential role, but not the sole role in the EOT effect.

It has been demonstrated that quasicylindrical waves together with SPPs are generated by slit or hole scattering of light on an interface of a metallic grating [19,20]. SPPs contribute dominantly to surface wave intensity for wavelengths smaller than 1 μm for noble metals [20], also cross conversion between the two surface waves has been observed [21].

Besides their wide applications in experimental nano optics and optics technology, metallic gratings are also frequently used to study the Wood's anomaly. This phenomenon was discovered by Wood [22] more than 100 years ago and refers to an abrupt change in intensity of diffraction orders at certain wavelengths for a metallic grating. A first theoretical explanation of Wood's anomalies was given by Rayleigh [23], making the conjecture that an anomaly occurs when a diffraction order grazes the surface of the grating and, in consequence, is passing off in the far field, while it still exists as an evanescent wave in the grating near field. The wavelength corresponding to a passing off of a grating order is called a Rayleigh wavelength and follows from the well-known grating formula. Later on, Fano [24] described Wood's anomaly to be comprised of two coupled phenomena: first, an edge or Rayleigh anomaly showing as a sharp edge in the spectral intensity at the Rayleigh wavelength and, second, a diffuse anomaly also first observed by Wood, including a minimum and, in close spectral proximity to it, a maximum of spectral intensity [25].

It is accepted that Wood's anomaly causes the EOT phenomenon [18]. Mostly the steady-state interaction under continuous-wave excitation has been studied. In this paper, an ultrashort illumination of a 1D grating and the temporal and spectral near-field features are presented. To obtain the presented numerical results, the Maxwell's equations are solved based on the grating geometry and the Drude model for electron dynamics in the grating material. The numerical results show that whether or not the grating is formed on a substrate is important to the features of Wood's anomaly in the near field. The carrier wavelength of the incident pulse is selected to be at a typical Ti:sapphire wavelength. A finite difference time domain (FDTD) code is used for the numerical calculations [26].

II. THE THEORETICAL MODEL

With reference to Figs. 1(a) and 1(b), a freestanding grating in air and a grating on a dielectric substrate with a refractive index n_s are studied. The former case resembles a setup frequently used in theoretical models explaining the underlying optical principles while the latter represents a typical experimental setup. A comparison of both reveals how the light transmission is influenced by the dielectric support. In the model, the electric field of the exciting light pulse oscillates

---

[*] j.bethge@vossiusandpartner.com

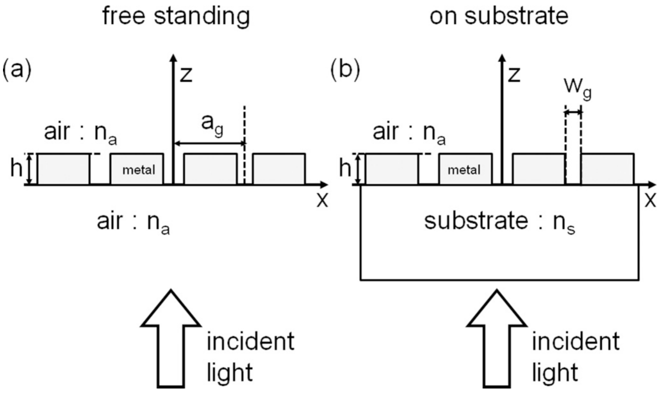

FIG. 1. (a) A freestanding grating, i.e., the index of refraction above and below $n_a = 1$. (b) A grating supported by a dielectric substrate $n_s = 1.1$ with air on the top. In both setups, the pitch length of the grating is $a_g = 750$ nm, the thickness of the gold film is $h = 120$ nm, and the width of a grating slit is $w_g = 60$ nm.

parallel to the x axis and its wave vector is directed in the z direction, normal to the bottom of the grating, i.e., TM polarization is used. The incident field is simulated by a plane wave at $\lambda_0 = 810$ nm, i.e., $\nu_0 \approx 0.37$/fs, modulated with a Gaussian temporal shape.

Frequency-dependent values for the real and imaginary parts of the metal permittivity ϵ_m of the gold surface close to ν_0 are calculated based on Ref. [27], i.e., $\epsilon_{m,\mathrm{re}} \approx -25$ and $\epsilon_{m,\mathrm{im}} \approx 1.6$. The upper and lower interface each have a SPP resonance. With an increasing difference in the refractive index on said interfaces, the frequency spacing of said resonances will also increase. To simultaneously excite both SPP resonances at a comparable level of field intensity, a sufficiently broad excitation bandwidth is needed.

The first-order SPP resonances at the air/metal and the substrate/metal interfaces are given by $\nu_{\mathrm{SP},a} \approx \nu_{R,a}(1 + [2\epsilon_{m,\mathrm{re}}]^{-1})$ and $\nu_{\mathrm{SP},s} \approx \nu_{R,s}(1 + [2\epsilon_{m,\mathrm{re}}]^{-1})$ where $\nu_{R,a} = c/a_g$ and $\nu_{R,s} = \nu_{R,a}/n_s$ denote the first-order Rayleigh frequencies with $a_g = 0.75\ \mu$m being the grating period or pitch length. The above SPP resonances are derived from the SPP dispersion relation of light on a smooth metallic surface [6]. Since $\epsilon_{m,\mathrm{re}}$ is a large negative number, the first-order SPP resonances are near to the first-order Rayleigh anomalies.

In the present paper, a refractive index for the substrate of $n_s = 1.1$ is used. For some glass types, the refractive index can be as low as $n = 1.35$. However, a simultaneous excitation of both SPP resonances would require a Gaussian pulse duration smaller than $\delta t_p = 0.44/(\nu_{R,a} - \nu_{R,s}) \approx 4.2$ fs. Since δt_p is antiproportional to $\nu_{R,a} - \nu_{R,s}$ for a silica substrate with $n_s = 1.5$, even shorter pulses would be required. Such short pulses are rather difficult to use experimentally, furthermore, numerical calculations become increasingly computationally demanding for shorter pulses when a FDTD method is used.

A refractive index $n_s = 1.1$ for the substrate corresponds to a pulse duration of $\delta t_p \approx 12$ fs. To sufficiently excite both resonances in this paper, the exciting pulse width (FWHM of pulse intensity) is set to $t_p = 10$ fs. A refractive index difference of 0.1 is experimentally relevant, e.g., when on one interface of the grating an additional coating or liquid is deposited [28,29]. To measure the respective output fields and their power spectra, near-field scanning optical microscopy would be a suitable experimental tool [7].

The numerical calculations of the pulse propagation were performed with a FDTD code applied to Maxwell's equations for the only nonvanishing magnetic component, H_y and the two electric field components E_x, E_z. The code is described in Refs. [9,30]. To calculate the transmission, the incident pulse is numerically propagated through the grating by solving the Maxwell's equations. To account for electron dynamics in the metal of the grating, the Maxwell's equations are combined with Drude's equations. The mathematical description for the freestanding grating can be found, e.g., in Ref. [31]. Including the description of the grating deposited on a substrate, we arrive at the following set of equations:

$$-\frac{\partial H_y}{\partial z} = \epsilon_0 \epsilon \frac{\partial E_x}{\partial t} + J_x, \tag{1}$$

$$\frac{\partial H_y}{\partial x} = \epsilon_0 \epsilon \frac{\partial E_z}{\partial t} + J_z, \tag{2}$$

$$\mu_0 \frac{\partial H_y}{\partial t} = \frac{\partial E_z}{\partial x} - \frac{\partial E_x}{\partial z}, \tag{3}$$

$$\frac{\partial \vec{J}}{\partial t} + \gamma_D \vec{J} = \epsilon_0 \omega_D^2 \vec{E}. \tag{4}$$

The above equation system consists of the Maxwell's equations, Eqs. (1)–(3), coupled to the auxiliary equation, Eq. (4), related to the motion of the quasifree charged particles in the metal. ϵ_0 and μ_0 are the free-space permittivity and magnetic permeability, respectively. ϵ is the relative permittivity, i.e., $\epsilon = 1$ for the freestanding grating. For the electromagnetic field in the substrate $\epsilon = n_s^2 = 1.21$ is calculated. The metal polarization $\vec{P}_m$ is represented by its time derivative $\vec{J} = \partial \vec{P}_m/\partial t$. The values $J_{x,z}$ follow from the Drude model and are correlated to the above-mentioned complex metal permittivity ϵ_m, via the parameters ω_D and γ_D of Eq. (4) according to the expression $\epsilon_m(\omega) = 1 - \omega_D^2/(\omega^2 + i\gamma_D\omega)$. The incorporation of Eq. (4) into the fundamental Yee's leap-frog algorithm scheme of our theoretical model follows instructions given in Ref. [30].

The wave-vector components in the x-z plane are given by $k_{x,q} = qG_x$ and $k_{z,q} = \sqrt{k^2 - k_{x,q}^2}$, where $k = \frac{\omega}{c}$ is the free-space wave number, $q = 0, \pm1, \ldots$ denotes the diffraction order of the grating modes, and $G_x = 2\pi/a_g$ is the reciprocal lattice vector. We relate the zero-order mode, $q = 0$, to a propagating wave directed along the z axis ($k_x = 0$), frequently described as specular transmission mode. On the other hand, the first-order modes, $q = +1$ and $q = -1$, are associated with SPP waves in view of the z axis while propagating along the positive and negative x axis. These SPP waves appear if the condition $k^2 - G_x^2 < 0$ is met, that is, for $\nu < \nu_{R,a}$.

III. THE TEMPORAL EVOLUTION OF THE GRATING NEAR FIELD

It is of interest how the light field evolves with time at a few nanometers above the grating ($z = h + 8$ nm) at various transverse locations, namely, $x = 0$, $x = a_g/4$, and $x = a_g/2$, with $x = 0$ corresponding to the center of a slit. In Fig. 2, magnetic fields are shown on a delay axis for the freestanding

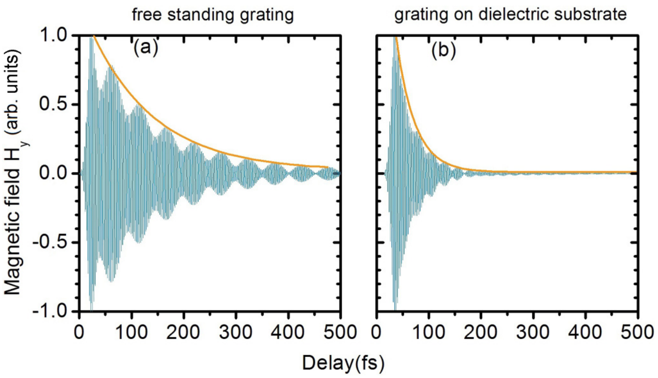

FIG. 2. Amplitude of the magnetic field for (a) the freestanding grating and (b) the grating supported by the dielectric, both at $x = a_g/2$ and at $z = h + 8$ nm, excited with a 10 fs light pulse. Also a fitted exponential decay (red curve) is shown connecting the amplitude peaks.

grating in Fig. 2(a) and with dielectric support in Fig. 2(b) at the center of the metallic section, i.e., at $x = a_g/2$. In Fig. 2 and all subsequent figures, zero delay refers to the arrival of the pulse center, i.e., of the maximum intensity, of the incident pulse on the grating surface. Damped magnetic field oscillations are observed for both gratings, starting with a distinct sharp peak originated from the short incident pulse. The response of the excited grating following the initial peak appears in the form of a high-frequency oscillation with a superimposed slow amplitude. Comparing Figs. 2(a) and 2(b) differences for the decay time of the oscillation t_d and the modulation period t_m are found, wherein the modulation period refers to a time interval between subsequent modulation peaks. The peaks of the amplitude are connected by the red curve, which is best described by an exponential decay. With an exponential decay parameter $t_d \approx 123$ fs for the freestanding grating and $t_d \approx 36$ fs on the dielectric support. In other words, the transmitted field amplitude of the grating on the dielectric support drops three to four times faster. The increased detuning of the two SPP oscillators gives rise to a faster decay of the transmitted field amplitude. The loss of field energy is due to higher radiation into the outside and absorption in the metal.

Moreover, the modulation period of the grating on a dielectric substrate $t_m \approx 25$ fs is smaller than that of a freestanding grating $t_m \approx 48$ fs. This can be explained with a larger spectral width in the former case being available due to the stronger damping.

The amplitude modulation in Fig. 2 can be described in terms of a modulation index m. In radio frequency, engineering m is used to measure amplitude variations caused by an audio signal impressed onto a high-frequency carrier. An algebraic expression of m can be found in Ref. [32] and Fig. 3 shows m for different modulation periods p. m approaches a maximum value of $m = 1$ when the interfering waves have a similar amplitude and phase. Thus, m is an indicator for the relative amplitude dynamics.

For the freestanding grating, a continuous increase of m is observed. The peak value of $m \approx 0.95$ is reached at about $t = 500$ fs, i.e., after nine modulation periods. The amplitude modulation at the beginning of the modulation process is characterized by a low value of m corresponding to different amplitudes of the interfering modes. This difference becomes smaller with increasing p and the wave tends to become fully modulated.

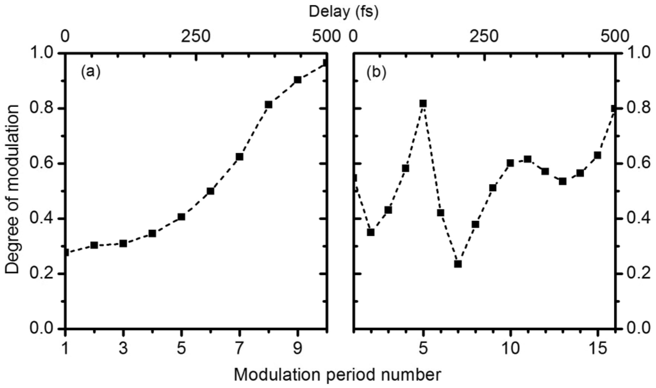

FIG. 3. The degree of modulation m of the amplitude for different modulation periods p.

In contrast for the grating on a substrate, the m curve has a short deterioration at the beginning showing a first increase to a peak value of $m \approx 0.8$ at about $t = 150$ fs. Afterward, m shows a steep decrease followed by a moderate increase up to about $m = 0.6$, followed by a slow decrease, and finally arriving at $m = 0.8$. The variations of the magnetic field in Fig. 2 are due to a self-modulation of the field amplitude following the impact of a short pulse. It is noted that the amplitude modulation of H_y is a linear process connected with radiation out of the grating.

Figure 4 shows the envelopes of the magnetic field at $x = 0$, $x = a_g/4$, and $x = a_g/2$, respectively. The envelopes are derived via Fourier filtering of H_y. At location $x = a_g/4$, the magnetic field amplitude is at all times smaller than at $x = 0$ and $x = a_g/2$. According to the model of Ref. [31], the zero-order mode ($q = 0$) is a propagating wave directed in the z direction and the two other modes ($q = 1$ and $q = -1$) are evanescent SPP waves decaying with z and, simultaneously, propagate along x. This gives rise to an interference between

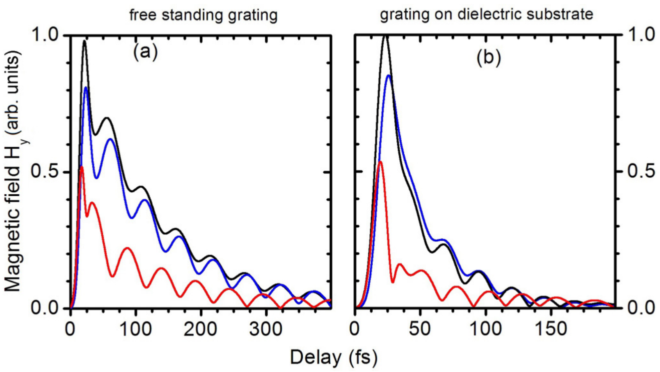

FIG. 4. Envelopes of the magnetic field for the two grating types at $z = h + 8$ nm and at different transverse locations on the upper grating air/metal interface: $x = 0$ (black line), $x = a_g/4$ (red), and $x = a_g/2$ (blue), cf. Fig. 1. The red curves have been enlarged by a factor of 5. The modulation period in (a) $t_m \approx 48$ fs and in (b) $t_m \approx 25$ fs.

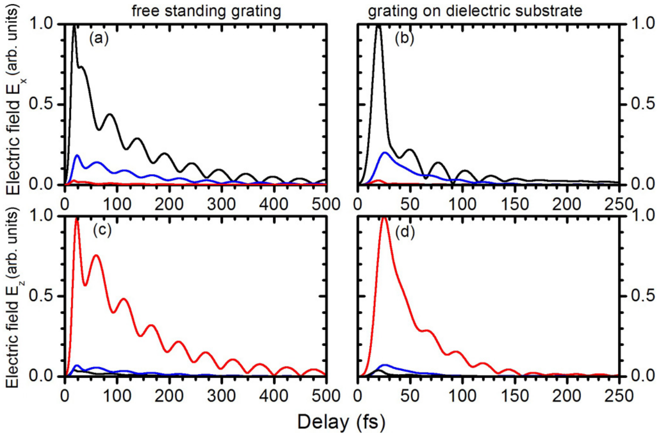

FIG. 5. Envelopes of the electric fields E_x (top line) and E_z (bottom line) at $z = h + 8$ nm, at different transverse locations: $x = 0$ (black line), $x = a_g/4$ (red), and $x = a_g/2$ (blue), cf. Fig. 1.

the counterpropagating waves, e.g., a node at $x = a_g/4$ appears. At this location, as a result of the interference, the strong first order waves disappear, while the weak zeroth-order mode, i.e., the red curve, becomes visible. Comparing Figs. 4(a) and 4(b), a shorter decay time $t_d \approx 36$ fs and a shorter modulation period $t_m \approx 25$ fs is observed for the grating on a dielectric substrate.

Figure 5 shows the electric field envelopes of the two electric components E_x (top) and E_z (bottom).

Figures 5(a) and 5(b) show that the amplitudes of the E_x component at $x = 0$ (black line) is at all times larger than the respective amplitude at $x = a_g/4$ and $x = a_g/2$. Figures 5(c) and 5(d) show that the amplitudes of the E_z component at $x = a_g/4$ (red line) is at all times larger than the respective amplitude at $x = 0$ and $x = a_g/2$. The relative difference in the amplitudes between E_x and E_z at different x positions can be explained by the different boundary conditions on the metal and in the opening. The relative E_x amplitudes at the respective x positions correspond with those of the respective H_y components as shown in Figs. 4(a) and 4(b).

IV. TIME-RESOLVED SPECTRA OF THE MAGNETIC NEAR FIELD

In the following, spectral dynamics over time of H_y are discussed based on a wavelet transform [33]. The wavelet transformation is a well-established method for analyzing a complex temporal and spectral evolution of an electromagnetic field. For the wavelet transform $W(u, s)$, a Gabor wavelet ψ is used. Hereinafter, the analysis is restricted to an analysis of the moduli $A_W = |W(u, s)|$ as introduced in Ref. [31]. The wavelet transform is given by

$$W(u, s) = \frac{1}{\sqrt{s}} \int_{-\infty}^{\infty} H_y(t)\psi^*[(t-u)/s]dt, \tag{5}$$

with the Gabor wavelet from Refs. [31,33]:

$$\psi(t) = \frac{1}{(\sigma^2\pi)^{1/4}} e^{-t^2/2\sigma^2 + i\eta t}, \tag{6}$$

with W being a complex function of the two variables u and s, which are referred to as the translation and scaling parameters.

Figure 6 shows two spectrograms of the moduli A_W in the u/s plane for the magnetic field of the freestanding grating, Fig. 6(a), and on a substrate, Fig. 6(b). Note that s is inverse to the frequency ν, thus an aditional frequency axis is shown to improve the intelligibility of the transformation $s = \nu_{\mathrm{SP},a}/\nu$. To simplify the comparison between the spectrograms, some prominent frequencies are identified.

Due to the time and frequency spread of the Gabor wavelet ψ, the time and frequency coordinates in the above

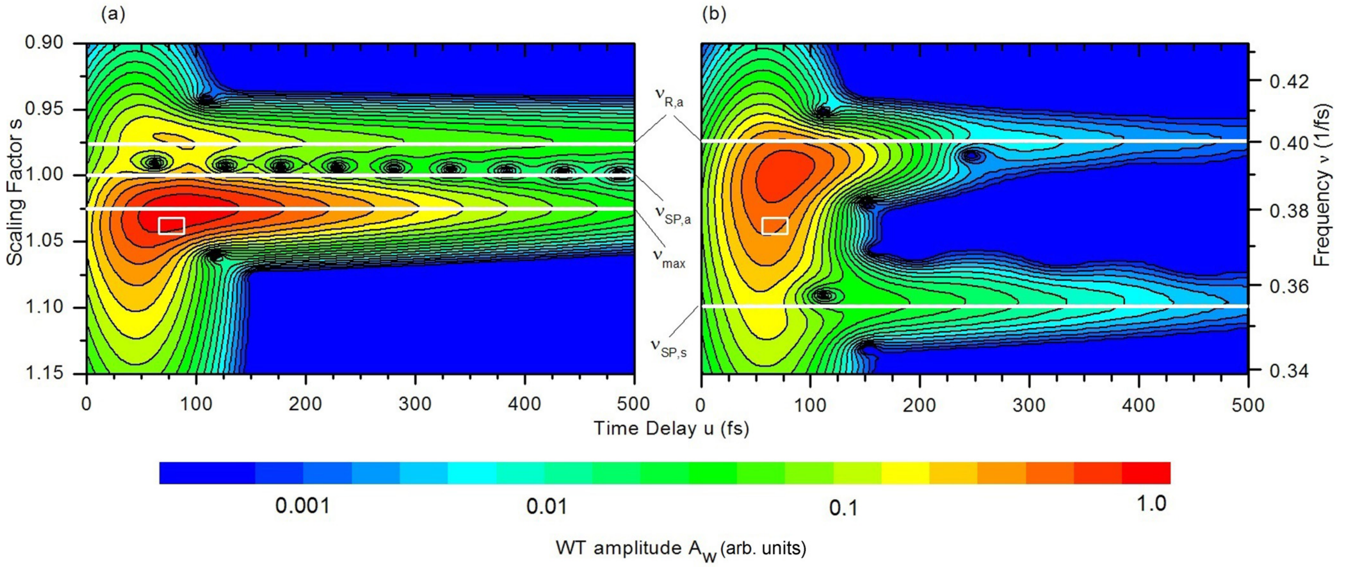

FIG. 6. Contour plots of the modulus $A_W = |W(u, s)|$ of a Gabor wavelet-transform of the H_y field component in the u/s plane for a freestanding grating (a) and a grating on a dielectric substrate (b). The white rectangles illustrate local Heisenberg boxes indicating the minimum spectral and temporal spread in the time-frequency plane.

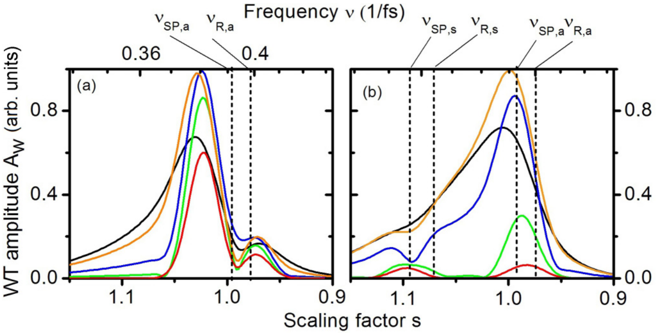

FIG. 7. The two graphs display the modulus A_W vs. the scaling factor s (bottom) and the frequency (top) based on the contour plots Figs. 6(a) and 6(b) for (a) the freestanding grating and (b) the grating on the substrate. Curves relate to different translation parameters u (time delay): $u = 50$ fs (black), $u = 75$ fs (orange), $u = 100$ fs (blue), $u = 150$ fs (green), and $u = 200$ fs (red). The vertical broken lines highlight the spectral locations of the Rayleigh frequencies ($\nu_{R,a}$, $\nu_{R,s}$) and SPP resonances ($\nu_{\mathrm{SP},a}$, $\nu_{\mathrm{SP},s}$).

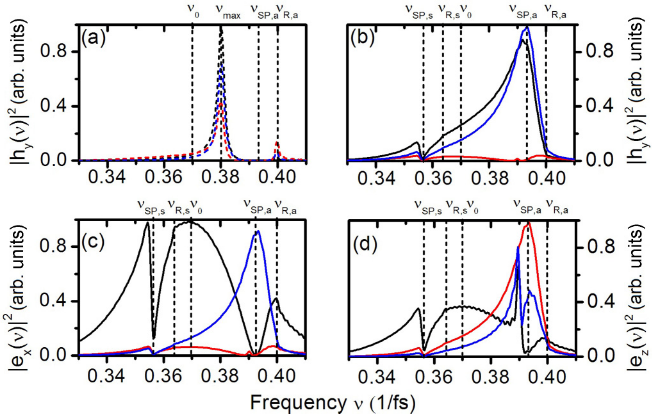

FIG. 8. Numerically calculated spectral intensities of the near field at $z = h + 8$ nm at $x = 0$ (black), $x = a_g/4$ (red), and $x = a_g/2$ (blue). In (a), $|h_y|^2$ for the freestanding grating and in (b), (c), and (d) $|h_y|^2$, $|e_x|^2$, and $|e_z|^2$ for the grating on a support are shown. The red curves in (a), (b), and (c) are enhanced by a factor of 100.

spectrograms cannot be specified to an accuracy better than $\sigma_t = s\sigma/\sqrt{2}$ and $\sigma_\omega = 1/(\sqrt{2}s\sigma)$, with $\sigma = 30$ fs being the full temporal width of the Gaussian window function used in the wavelet transform.

In Fig. 6(a), i.e., for the freestanding grating, a peak of A_W is observed followed by a long decrease. In contrast, in Fig. 6(b), the initial peak is followed by a much faster decrease, which corresponds to the faster decrease of the field amplitude observed for the grating on a dielectric support in Fig. 2(b).

Furthermore, in Fig. 6(a) between $\nu_{R,a}$ and $\nu_{\max}$, a complex evolution of the amplitudes is observed. For a more detailed analysis, Figs. 7(a) and 7(b) show cuts, perpendicular to the u axis, of the spectrograms of Figs. 6(a) and 6(b), respectively.

One recognizes that A_W between $\nu_{R,a}$ and $\nu_{\max}$ in Fig. 7(a), i.e., for the freestanding grating, exhibits a Fano-type profile. The sharp anomaly at $\nu_{R,a}$ is followed by an antiresonance transmission dip, with a respective minimum close to $\nu_{\mathrm{SP},a}$, followed by a respective peak. This indicates a narrow coupling between the SPPs and the Rayleigh anomaly. In contrast, for the grating on a dielectic support, i.e., in Fig. 7(b), no such profiles are observed. Instead, more complex spectra are found, which are explained by two different SPP resonances $\nu_{\mathrm{SP},a}$ and $\nu_{\mathrm{SP},s}$. The second SPP resonance at $\nu_{\mathrm{SP},s}$ leads to a significantly extended transmission frequency range.

V. POWER SPECTRA OF THE MAGNETIC AND ELECTRIC NEAR FIELDS

This chapter presents the spectral intensities (power spectra) $|h_y(\nu)|^2$, $|e_x(\nu)|^2$, and $|e_z(\nu)|^2$ of the magnetic near field and its two corresponding electric components obtained via respective Fourier transforms, e.g., $|h_y(\nu)|^2 = |\int_{-\infty}^{\infty} H_y(t)\exp(-i2\pi\nu t)dt|^2$.

Figure 8(a) shows the numerically calculated near-field power spectrum of $|h_y(\nu)|^2$ for the freestanding grating and Figs. 8(b), 8(c) and 8(d) show the respective spectra for each of the above field components for the grating on the dielectric substrate. Each spectrum exhibits a plurality of resonance peaks and antiresonance dips. Among them are pairs of dips and peaks that constitute characteristic Fano-type profiles.

In Fig. 8(a), one observes two peaks, one at $\nu_{\max} = 0.38$/fs, another at $\nu_{R,a} = 0.40$/fs, and a region of low intensity therein betweeen. The minimum of the gap is close to $\nu_{\mathrm{SP},a}$. In other words, this compound resonance system comprises a sharp anomaly at $\nu_{R,a}$, a dip around $\nu_{\mathrm{SP},a}$, and a peak at $\nu_{\max}$, which constitute a Fano profile as described above. Moreover, one notes a slightly faster increase at the high-frequency side of the peak (beyond $\nu_{\max}$), indicating an asymmetric resonance curve, which is in a qualitative accordance with experimental and theoretical results, e.g., Ref. [7].

In contrast, for the grating on a dielectric, two SPP resonances must be considered and two Fano-type profiles may occur. In Fig. 8(c), starting from the high-frequency side, the black line exhibits an edge at $\nu_{R,a}$, i.e., a sharp anomaly, followed by an antiresonance dip at $\nu_{\mathrm{SP},a}$ and then grows onto a peak. A second edge at $\nu_{R,s}$ indicates a second sharp anomaly, followed by an antiresonance dip at $\nu_{\mathrm{SP},s}$ and a resonance peak further away. In other words, two sharp anomalies are followed by a diffuse anomaly, respectively, which confirms the presence of two Fano-type profiles, one at $\nu_{\mathrm{SP},a}$ and the other one at $\nu_{\mathrm{SP},s}$. While the diffuse anomaly close to $\nu_{\mathrm{SP},s}$ has a distinctive antiresonance and a resonance pattern, the diffuse anomaly at $\nu_{\mathrm{SP},a}$ is either an antiresonance dip [black curve in Fig. 8(c)] followed by a peak or a resonance peak followed by a dip [red curve in Fig. 8(d)].

In conclusion, in all spectral curves the edge, i.e., the sharp resonance, is followed by a diffuse anomaly. The difference in the appearance of the diffuse anomaly is associated with different Fano line-shape parameters [34].

VI. A LOOK TOWARD THE FAR FIELD TRANSMISSION

Figure 9 shows the electric transmission spectrum $|e_x(\nu)|^2$ taken at a distance to the grating of 3.5 μm, that is at about 4.3 times the carrier wavelength. Note that the same parameters have been employed as in Fig. 8(c) except for the distance to the grating. In contrast to near-field curves of Fig. 8(c)

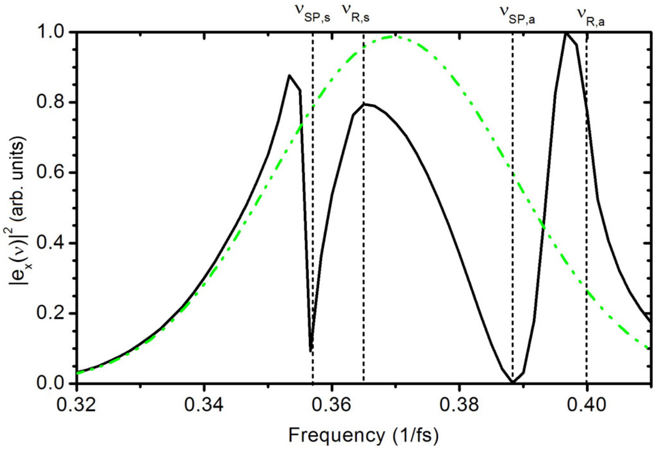

FIG. 9. Spectral power of the electric field vs frequency at $z = h + 3.5\ \mu$m for the grating on the dielectric substrate. The frequencies of the Rayleigh anomalies and the SPP resonances are marked as vertical lines. The green curve relates to the normalized power spectrum of the incident light pulse.

at a distance of about 8 nm to the grating, in Fig. 9 a distinguishing between the spectra is not possible since all spectra are identical, therefore Fig. 9 shows only the $|e_x(\nu)|^2$ component. In particular, a strict correspondence in respect to the spectral position of the minima and maxima of the curves can be verified. Therefore, it follows that near-field contributions of the SPP dynamics to transmission spectra have almost disappeared at 3.5 μm. Thus, the spectrum at 3.5 μm already has the features of a far-field spectrum. Said spectrum is consistent with the far-field spectrum of Ref. [16], which has minima close to the SPP resonances and maxima close to the Rayleigh anomalies.

VII. CONCLUSIONS

Based on a numerical solution of Maxwell's equations, the light field dynamics in two different metallic grating setups with one-dimensional subwavelength slit apertures, namely, a freestanding grating in air and a grating on a dielectric substrate have been studied. In a subwavelength distance and at a timescale in the same order of the pulse duration, the grating transmission is found to be influenced by the presence of a substrate.

In the time domain, the main difference is found to be a faster decay and a lower degree of modulation of the amplitude for the grating on the substrate. A wavelet transform has been used to calculate the corresponding temporal-spectral features.

In the spectral domain, for the freestanding grating a single Fano-type profile corresponding to a single Rayleigh anomaly at the air/metal interface is observed. For the grating on the substrate two Fano-type profiles are observed, one at the air/metal SPP resonance and the other at the substrate/metal SPP resonance. On one hand, the diffuse anomaly at the substrate/metal SPP resonance is formed by a distinctive antiresonance and a resonance pattern. On the other hand, the diffuse anomaly at the air/metal SPP resonance is found to be either an antiresonance dip followed by a peak or a resonance peak followed by a dip, depending on the respective transverse location.

Furthermore, it is found that for larger distances and longer delays, the contributions of the surface dynamics vanish, which eventually leads to the well-known transmission spectra of the classical grating theory.

ACKNOWLEDGMENTS

The technical assistance of N. Raabe and L. von Grafenstein are gratefully acknowledged.

---

[1] D. Pines and D. Bohm, Phys. Rev. **85**, 338 (1952).
[2] R. H. Ritchie, Phys. Rev. **106**, 874 (1957).
[3] H. Raether, *Surface Plasmons on Smooth and Rough Surfaces and on Gratings*, Springer Tracts in Modern Physics (Springer, Berlin, 2006).
[4] W. L. Barnes, A. Dereux, and T. W. Ebbesen, Nature **424**, 824 (2003).
[5] T. W. Ebbesen, H. J. Lezec, H. F. Ghaemi, T. Thio, and P. A. Wolff, Nature **391**, 667 (1998).
[6] H. F. Ghaemi, T. Thio, D. E. Grupp, T. W. Ebbesen, and H. J. Lezec, Phys. Rev. B **58**, 6779 (1998).
[7] C. Genet, M. P. van Exter, and J. P. Woerdman, Opt. Commun. **225**, 331 (2003).
[8] M. Sarrazin, J.-P. Vigneron, and J.-M. Vigoureux, Phys. Rev. B **67**, 085415 (2003).
[9] R. Müller, V. Malyarchuk, and C. Lienau, Phys. Rev. B **68**, 205415 (2003).
[10] R. Müller, C. Ropers, and C. Lienau, Opt. Express **12**, 5067 (2004).
[11] W. L. Barnes, W. A. Murray, J. Dintinger, E. Devaux, and T. W. Ebbesen, Phys. Rev. Lett. **92**, 107401 (2004).
[12] H. Lochbihler, Phys. Rev. B **50**, 4795 (1994).
[13] J. A. Porto, F. J. García-Vidal, and J. B. Pendry, Phys. Rev. Lett. **83**, 2845 (1999).
[14] U. Schröter and D. Heitmann, Phys. Rev. B **58**, 15419 (1998).
[15] D. S. Kim, S. C. Hohng, V. Malyarchuk, Y. C. Yoon, Y. H. Ahn, K. J. Yee, J. W. Park, J. Kim, Q. H. Park, and C. Lienau, Phys. Rev. Lett. **91**, 143901 (2003).
[16] J. M. Steele, C. E. Moran, A. Lee, C. M. Aguirre, and N. J. Halas, Phys. Rev. B **68**, 205103 (2003).
[17] D. J. Park, K. G. Lee, H. W. Kihm, Y. M. Byun, D. S. Kim, C. Ropers, C. Lienau, J. H. Kang, and Q.-H. Park, Appl. Phys. Lett. **93**, 073109 (2008).
[18] D. de Ceglia, M. A. Vincenti, M. Scalora, N. Akozbek, and M. J. Bloemer, AIP Adv. **1**, 032151 (2011).
[19] F. van Beijnum, C. Retif, C. B. Smiet, H. Liu, P. Lalanne, and M. P. van Exter, Nature **492**, 411 (2012).
[20] X. Zhang, H. Liu, and Y. Zhong, Phys. Rev. B **89**, 195431 (2014).
[21] X. Y. Yang, H. T. Liu, and P. Lalanne, Phys. Rev. Lett. **102**, 153903 (2009).
[22] R. W. Wood, Phys. Rev. **48**, 928 (1935).
[23] L. Rayleigh, London, Edinburgh, Dublin Philos. Mag. J. Sci. **14**, 60 (1907).
[24] U. Fano, J. Opt. Soc. Am. **31**, 213 (1941).

[25] S. Enoch and N. Bonod, *Plasmonics: From Basics to Advanced Topics*, Springer Series in Optical Sciences (Springer, Berlin, 2012).

[26] A. Taflove and S. C. Hagness, *Computational Electrodynamics: The Finite-Difference Time-Domain Method*, Antennas and Propagation Library No. Bd. 1 (Artech House, Boston, 2000).

[27] P. B. Johnson and R. W. Christy, Phys. Rev. B **6**, 4370 (1972).

[28] A. Krishnan, T. Thio, T. J. Kim, H. J. Lezec, T. W. Ebbesen, P. A. Wolff, J. Pendry, L. Martin-Moreno, and F. J. Garcia-Vidal, Opt. Commun. **200**, 1 (2001).

[29] J. M. McMahon, J. Henzie, T. W. Odom, G. C. Schatz, and S. K. Gray, Opt. Express **15**, 18119 (2007).

[30] S. A. Cummer, IEEE Trans. Antennas Propag. **45**, 392 (1997).

[31] R. Müller and J. Bethge, Phys. Rev. B **82**, 115408 (2010).

[32] F. E. Terman, *Radio Engineers' Handbook* (Mc Graw-Hill Book Company, New York, 1943), p. 531.

[33] S. Mallat, *A Wavelet Tour of Signal Processing*, 2nd ed. (Academic Press, San Diego, 2001).

[34] A. E. Miroshnichenko, S. Flach, and Y. S. Kivshar, Rev. Mod. Phys. **82**, 2257 (2010).